

Radiative shock solutions with grey nonequilibrium diffusion

Robert B. Lowrie · Jarrod D. Edwards

Received: 11 October 2007 / Revised: 4 March 2008 / Accepted: 30 April 2008 / Published online: 30 May 2008
© Springer-Verlag 2008

Abstract This study describes a semi-analytic solution of planar radiative shock waves with a grey nonequilibrium diffusion radiation model. The solution may be used to verify radiation-hydrodynamics codes. Comparisons are made with the equilibrium diffusion solutions of Lowrie and Rauenzahn (Shock Waves 16(6):445–453, 2007). The solution also gives additional insight into the structure of radiative shocks. Previous work has assumed that the material temperature reaches its maximum at the post-shock state of the embedded hydrodynamic shock (Zel’dovich spike). We show that in many cases, the temperature may continue to increase after the hydrodynamic shock and reaches its maximum at the isothermal sonic point. Also, a temperature spike may exist even in the absence of an embedded hydrodynamic shock. We also derive an improved estimate for the maximum temperature.

Keywords Radiative shocks · Radiation hydrodynamics · Code verification

PACS 52.35.Tc · 43.25.Qp

1 Introduction

This study describes a semi-analytic solution for planar radiative shocks with a grey nonequilibrium diffusion

radiation model. It is an extension of the work of Lowrie and Rauenzahn [13] who considered solutions in the equilibrium diffusion limit. The solutions described here are accurate enough to be used to verify radiation hydrodynamics codes that may use the nonequilibrium diffusion radiation model (e.g., see Refs. [2, 8, 9]). The solution procedure requires finding numerically the root of a polynomial and integrating a pair of coupled nonlinear ordinary differential equations. Because a numerical procedure is still required, we refer to our solutions as “semi-analytic.”

The classic physical description of radiative shocks is given by Zel’dovich [20], Zel’dovich and Raizer [21], and Mihalas and Mihalas [14]. For an optically-thick shock, which we also assume here, a more detailed picture has been given recently by Drake [4–6]. Aside from the work of Refs. [1, 3, 13] that addresses the equilibrium diffusion limit, analytical treatments in past work typically assume low energy density; specifically, they assume that material energy dominates the radiation energy throughout the domain [5, 6, 10, 17].

In this study, we consider the (very) high energy density regime, which we define to include the radiation energy and pressure terms in the total energy and momentum budgets. We realize that the radiation treatment that we employ here is a simple nonequilibrium model which for many conditions, is invalid for determining certain details of the radiative shock structure [4, 6, 7, 15, 16]. However, analytic solutions for problems in radiation hydrodynamics are very sparse. The solution described in this study is fairly easy to compute and may be used to test a subset of the physics algorithms within a full simulation code. The solution also offers insight into the shock structure. Previous work has assumed that the material temperature reaches its maximum at the post-shock state of the embedded hydrodynamic shock (Zel’dovich spike [20]). We show that in many cases, the temperature may

Communicated by C. Needham.

R. B. Lowrie (✉)
Computational Physics Group (CCS-2), Mail Stop D413,
Los Alamos National Laboratory, P. O. Box 1663,
Los Alamos, NM 87545, USA
e-mail: lowrie@lanl.gov

J. D. Edwards
Department of Nuclear Engineering, Texas A&M University,
College Station, TX 77843, USA

continue to increase after an embedded hydrodynamic shock and reaches its maximum at the isothermal sonic point.

The primary focus of this study is to extend the work of Ref. [13] to a grey nonequilibrium diffusion model, in order to generate solutions accurate enough for simulation code verification. This paper is organized as follows: In Sect. 2, we state the full governing equations that are solved. Section 3 defines the shock problem and reviews the structure of radiative shocks. The reduced set of equations solved is derived in Sect. 4 and the solution procedure is outlined in Sect. 5. Sample solutions are given in Sect. 6 and we derive a new estimate for the maximum temperature in Sect. 7.

2 Governing equations

In this study, most of the equations are expressed in nondimensional form. Dimensional quantities are denoted with a tilde; for example, \tilde{p} . The following dimensional quantities are used in the nondimensionalization:

\tilde{L}	(reference length)
$\tilde{\rho}_0$	(reference material mass density)
\tilde{T}_0	(reference material temperature)
\tilde{a}_0	(reference material sound speed)
\tilde{c}	(speed of light)
$\tilde{\alpha}_R$	(radiation constant)

where the subscript-“0” indicates that a variable is evaluated at the pre-shock state. The nondimensional quantities are then defined in terms of their dimensional counterparts as follows:

$x = \frac{\tilde{x}}{\tilde{L}}$	(spatial coordinate)
$t = \frac{\tilde{t}\tilde{a}_0}{\tilde{L}}$	(time coordinate)
$\rho = \frac{\tilde{\rho}}{\tilde{\rho}_0}$	(material mass density)
$v = \frac{\tilde{v}}{\tilde{a}_0}$	(material velocity)
$e = \frac{\tilde{e}}{\tilde{a}_0^2}$	(material internal specific energy)
$p = \frac{\tilde{p}}{\tilde{\rho}_0\tilde{a}_0^2}$	(material pressure)
$T = \frac{\tilde{T}}{\tilde{T}_0}$	(material temperature)
$\theta = \frac{\tilde{\theta}}{\tilde{T}_0}$	(radiation temperature)
$\sigma_a = \frac{\tilde{\sigma}_a\tilde{L}\tilde{c}}{\tilde{a}_0}$	(absorption cross section)

$$\sigma_t = \frac{\tilde{\sigma}_a\tilde{L}\tilde{c}}{\tilde{a}_0} \quad (\text{total cross section})$$

$$\kappa = \frac{\tilde{c}}{3\tilde{\sigma}_t\tilde{a}_0\tilde{L}} \quad (\text{radiation diffusivity}).$$

The radiation hydrodynamics model used in this study is the single-material, nonrelativistic Euler equations, coupled with grey nonequilibrium diffusion (see [14, Sect. 97]). We write this system in nondimensional form as

$$\partial_t \rho + \partial_x(\rho v) = 0, \quad (1a)$$

$$\partial_t(\rho v) + \partial_x \left(\rho v^2 + p + \frac{1}{3} \mathcal{P}_0 \theta^4 \right) = 0, \quad (1b)$$

$$\partial_t(\rho E) + \partial_x [v(\rho E + p)] = -\mathcal{P}_0 S_e, \quad (1c)$$

$$\partial_t \theta^4 + \frac{4}{3} \partial_x(v\theta^4) - \partial_x(\kappa \partial_x \theta^4) = S_e, \quad (1d)$$

where

$$S_e = \sigma_a(T^4 - \theta^4) + \frac{1}{3} v \partial_x \theta^4 \quad (2)$$

and E is the material specific total energy, defined as

$$E = e + \frac{1}{2} v^2. \quad (3)$$

The nondimensional constant \mathcal{P}_0 arises in the nondimensionalization process and is given by

$$\mathcal{P}_0 = \frac{\tilde{\alpha}_R \tilde{T}_0^4}{\tilde{\rho}_0 \tilde{a}_0^2}. \quad (4)$$

It is a measure of the influence of radiation on the flow dynamics; roughly speaking, \mathcal{P}_0 is proportional to the ratio of radiation pressure to material pressure and alternatively, the radiation energy to material energy.

The equations in the system (1) represent the conservation of mass, material momentum, material total energy, and radiation energy, respectively. The term S_e represents the transfer of energy between the radiation and material. The first term on the right-hand side of Eq. (2) represents radiation emission and absorption, while the second term is related to the work done by the radiation pressure on the material. The radiation energy, θ^4 , is measured in the comoving frame of the material [14, Sect. 95].

Several useful relations may be derived from the system (1). The sum of Eq. (1c) and \mathcal{P}_0 times (1d) gives the total energy relation

$$\begin{aligned} \partial_t(\rho E + \mathcal{P}_0 \theta^4) + \partial_x \left[v \left(\rho E + p + \frac{4}{3} \mathcal{P}_0 \theta^4 \right) \right] \\ = \mathcal{P}_0 \partial_x(\kappa \partial_x \theta^4), \end{aligned} \quad (5)$$

which implies that total energy (material plus radiation) is conserved. Strong solutions of the system (1) also satisfy

$$\rho \frac{De}{Dt} + p \partial_x v = \mathcal{P}_0 \sigma_a (\theta^4 - T^4). \quad (6)$$

For a given equation-of-state (EOS), the character of a shock wave is determined by the shock Mach number ($\mathcal{M}_0 = \tilde{v}_0/\tilde{a}_0 = v_0$), the parameter \mathcal{P}_0 , and the functions κ and σ_a . The Mach number determines the strength of the shock, while \mathcal{P}_0 measures the degree to which radiation affects the material dynamics.

Note that one can obtain the low energy density approximation by dropping the radiation pressure from Eq. (1b), along with the relativistic correction terms, which are those that contain products of v and θ in Eqs. (1d, 2, 5). However, dropping such terms is invalid whenever the post-shock conditions result in a local \mathcal{P} that is order unity.

In order to simplify the analysis further, several additional assumptions are made in this study. The absorption and total cross-sections are restricted to have the functional dependence $\sigma_a(\rho, T)$ and $\sigma_t(\rho, T)$ (so that $\kappa(\rho, T)$). In particular, we assume a homogeneous medium, so that the cross-sections have no explicit spatial dependence. We also assume a calorically perfect EOS, which for our nondimensionalization, is written as

$$p = \frac{\rho T}{\gamma}, \quad e = \frac{T}{\gamma(\gamma - 1)}, \quad (7)$$

where γ is assumed constant and represents the ratio of specific heats. This EOS is quite restrictive for several radiation-hydrodynamic flow regimes, but greatly simplifies the analysis. A more general EOS should be the subject of future work.

Although the solution presented here can be useful to help verify simulation codes and offers additional physical insight, the assumptions made must be kept in mind. As alluded to in the Introduction, the radiation model employed here may be far from an accurate description of the true radiation field. The grey assumption represents each cross section as a single frequency-averaged value; it is particularly invalid whenever the line structure of the material plays a significant role. Also, Eq. (1d) is the simplest nonequilibrium model and uses a constant Eddington factor of $1/3$ in the diffusion term, which assumes that the angular variation of the radiation is isotropic. Isotropy cannot be expected in flows with large gradients, such as within radiative shocks. We also have assumed that the ion and electron temperatures equilibrate instantaneously, and we have ignored heat conduction and viscous effects. In short, our assumptions certainly may break down. References [4, 6, 7, 15, 16] are examples where a more detailed physical picture of radiative shocks has been explored.

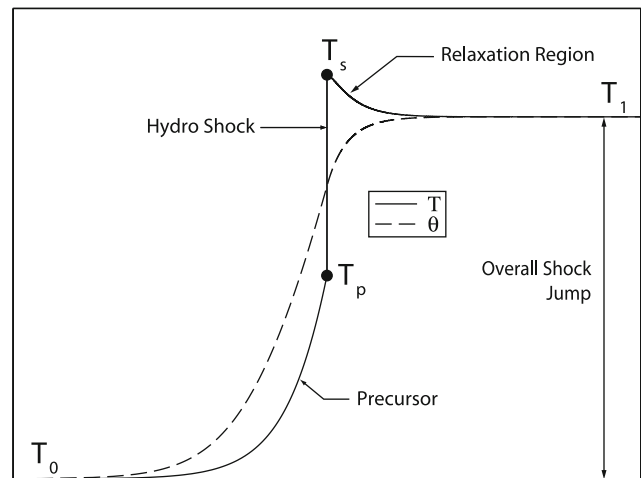


Fig. 1 Example subcritical shock profile of T and θ . The symbols denote the endpoints of an embedded hydrodynamic shock

3 Shock problem statement

This section defines the problem to be solved. As with the equilibrium diffusion system considered in Ref. [13], the system (1) is Galilean invariant. Then without a loss of generality, we can consider only the steady-state reference frame, where the shock speed is zero. The flow is assumed to move in the $+x$ direction. The reference state (subscript-0) will refer to the pre-shock conditions, attained as $x \rightarrow -\infty$, while the subscript-1 refers to post-shock conditions, attained as $x \rightarrow \infty$. See Fig. 1. We assume that far from the shock the flow is in radiative equilibrium ($\theta = T$). The problem statement is then as follows:

- *Given:* The values $\gamma, \mathcal{M}_0, \mathcal{P}_0$, and the functions $\sigma_a(\rho, T)$ and $\kappa(\rho, T)$. Note that the nondimensional pre-shock solution state is also known: $\theta_0 = 1, T_0 = 1, \rho_0 = 1$, and $v_0 = \mathcal{M}_0$.
- *Calculate:* The functions $\rho(x), v(x), T(x)$, and $\theta(x)$.

The classic picture for a shock temperature profile is shown in Fig. 1. This case is a subcritical shock, so that $T_p < T_1$, where T_p is the pre-hydro shock temperature. As a result of the diffusion term in Eq. (1d), θ is continuous through the shock. The post-hydro shock temperature is T_s , which then radiatively cools to T_1 in the relaxation region. A supercritical shock has $T_p \equiv T_1$. See Refs. [4–6, 13, 14, 21] for a more detailed discussion of this physical picture.

4 Reduced equations

In this section, we derive the reduced set of equations that satisfy the system (1) for the shock problem given in Sect. 3. We also describe certain properties of these equations.

4.1 Overall jump conditions

To determine state-₁ in Fig. (1), we use the overall jump conditions as in Ref. [13]:

$$\begin{pmatrix} \rho v \\ \rho v^2 + p^* \\ (\rho E^* + p^*)v \end{pmatrix}_0 = \begin{pmatrix} \rho v \\ \rho v^2 + p^* \\ (\rho E^* + p^*)v \end{pmatrix}_1, \quad (8)$$

where

$$p^* = p + \frac{1}{3}\mathcal{P}_0 T^4, \quad (9)$$

$$e^* = e + \frac{1}{\rho}\mathcal{P}_0 T^4, \quad (10)$$

$$E^* = e^* + \frac{1}{2}v^2. \quad (11)$$

These equations can be easily manipulated to a polynomial in T whose root must be found numerically; for the details, see Refs. [1, 13]. Note that in the low energy density approximation, the terms proportional to \mathcal{P}_0 are dropped, so that the above relations reduce to the standard hydrodynamic jump conditions. We will retain these terms in this study.

4.2 Hydrodynamic jump conditions

At a steady discontinuity, the system (1) gives the following jump relations separating state-_p from state-_s (see Fig. 1):

$$(\rho v)_p = (\rho v)_s, \quad (12a)$$

$$(\rho v^2 + p)_p = (\rho v^2 + p)_s, \quad (12b)$$

$$[v(\rho E + p)]_p = [v(\rho E + p)]_s, \quad (12c)$$

$$\left(-\kappa \partial_x \theta^4 + \frac{4}{3}v\theta^4\right)_p = \left(-\kappa \partial_x \theta^4 + \frac{4}{3}v\theta^4\right)_s. \quad (12d)$$

Note that θ is continuous across the jump, while ρ , v , p , and T may be discontinuous. The first three relations are the standard hydrodynamic jump conditions. Also, Eq. (12d) states that the diffusive flux (or comoving-frame flux [14]),

$$-\kappa \partial_x \theta^4,$$

is discontinuous at a shock. But the lab-frame flux,

$$-\kappa \partial_x \theta^4 + \frac{4}{3}v\theta^4,$$

is continuous. The jump in the comoving-frame flux at a hydrodynamic shock is a result of the jump in velocity; keep in mind that the shock reference frame is not a comoving frame.

4.3 Precursor and relaxation regions

In this section, we derive the ordinary differential equations that hold in the precursor and relaxation regions. In the

steady-state frame ($\partial_t \equiv 0$), integrate Eq. (1a) to give

$$\rho v = v_0 \equiv \mathcal{M}_0, \quad (13)$$

where \mathcal{M}_0 is the shock Mach number. For the EOS (7), the local Mach number is given by

$$\mathcal{M} = \frac{v}{\sqrt{T}} = \frac{\mathcal{M}_0}{\rho\sqrt{T}}. \quad (14)$$

Integrate Eq. (1b) to obtain

$$3\gamma \frac{\mathcal{M}_0^2}{\rho} + 3\rho T + \gamma \mathcal{P}_0 \theta^4 = K_m, \quad (15)$$

where the constant K_m is given by

$$K_m = 3(\gamma \mathcal{M}_0^2 + 1) + \gamma \mathcal{P}_0. \quad (16)$$

Equation (15) is quadratic in ρ and the solution is

$$\begin{aligned} \rho(T, \theta) &= \frac{K_m - \gamma \mathcal{P}_0 \theta^4 \pm \sqrt{(K_m - \gamma \mathcal{P}_0 \theta^4)^2 - 36\gamma \mathcal{M}_0^2 T}}{6T}. \end{aligned} \quad (17)$$

There are two roots or branches. The “-”-branch always satisfies $\rho(T_0, \theta_0) = \rho_0 = 1$. Which branch satisfies $\rho(T_1, \theta_1) = \rho_1$ is problem dependent. More discussion of the branch points will be given in the next section.

Next, integrate (5) and use (13) to yield

$$\theta' = v \frac{6C_p \rho(T-1) + 3\rho(v^2 - \mathcal{M}_0^2) + 8\mathcal{P}_0(\theta^4 - \rho)}{24\mathcal{P}_0 \kappa \theta^3} \quad (18)$$

where $C_p = 1/(\gamma - 1)$ and $(\cdot)' = d(\cdot)/dx$. Note that the corresponding expression for θ' is incorrect in Ref. [12, Eq. (18)]. Steady solutions of Eq. (6) satisfy

$$\rho v e' + p v' = \mathcal{P}_0 \sigma_a (\theta^4 - T^4), \quad (19)$$

which reduces to

$$\frac{\mathcal{M}_0}{\gamma} \left(C_p T' - \frac{T}{\rho} \rho' \right) = \mathcal{P}_0 \sigma_a (\theta^4 - T^4). \quad (20)$$

Differentiate Eq. (15) to obtain

$$-3\gamma \frac{\mathcal{M}_0^2}{\rho^2} \rho' + 3(\rho T' + T \rho') + 4\gamma \mathcal{P}_0 \theta^3 \theta' = 0, \quad (21)$$

or

$$\rho' = \rho^2 \frac{3\rho T' + 4\gamma \mathcal{P}_0 \theta^3 \theta'}{3(\gamma \mathcal{M}_0^2 - \rho^2 T)} \quad (22)$$

Substitute this expression into Eq. (20) to yield

$$T' = \left(\frac{\mathcal{P}_0}{3C_p \rho \mathcal{M}_0} \right) \left(\frac{Z_N}{\mathcal{M}^2 - 1} \right), \quad (23)$$

where

$$Z_N = 4\mathcal{M}_0 \theta^3 \theta' + (\gamma \mathcal{M}^2 - 1)r \quad (24)$$

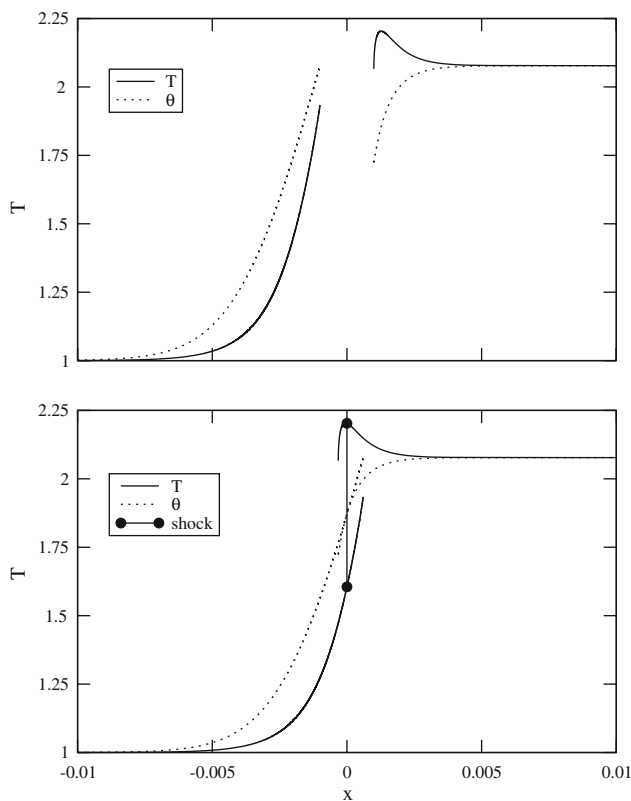


Fig. 2 Overview of the solution procedure. The *top plot* shows the precursor and relaxation branches; each is computed independently. These branches are then translated in x in such a way that they satisfy the hydrodynamic shock conditions at $x = 0$, as shown in the *bottom plot*. The portion of each branch that extends past the shock is then removed to form the final solution (see Fig. 8)

and

$$r = 3\rho\sigma_a(\theta^4 - T^4). \quad (25)$$

If we take $\theta' = 0$ (or assume low energy density), we have a similar expression for T' as one derived for recombination fronts by Williams and Dyson [19, Eq. (7)].

Equations (18) and (23) are two ordinary differential equations for θ and T . Knowing θ and T , we can find ρ from Eq. (17), p from Eq. (7), and v from Eq. (13).

4.4 Isothermal sonic point

From Eq. (17), there is a branch point in the solution whenever the discriminate vanishes, which occurs whenever

$$K_m - \gamma\mathcal{P}_0\theta^4 = \pm 6\mathcal{M}_0\sqrt{\gamma T}. \quad (26)$$

Substitute this expression back into Eq. (17) and recognize that only the “+”-root results in a nonnegative density, so that at the branch point

$$\rho = \mathcal{M}_0\sqrt{\frac{\gamma}{T}}. \quad (27)$$

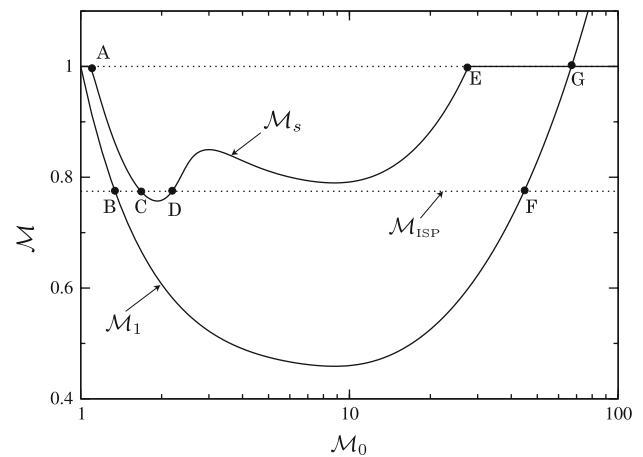


Fig. 3 \mathcal{M}_s and \mathcal{M}_1 versus \mathcal{M}_0 , for $\mathcal{P}_0 = 10^{-4}$, $\gamma = 5/3$, $\sigma_a = 10^6$, $\kappa = 1$. Labels A through G denote the transition points for the solution regimes discussed in Sect. 6. The labels are ordered by increasing \mathcal{M}_0

Using Eq. (13), this condition may be written in terms of the local Mach number as

$$\mathcal{M} = 1/\sqrt{\gamma} \equiv \mathcal{M}_{\text{ISP}}, \quad (28)$$

where we denote $\mathcal{M} = \mathcal{M}_{\text{ISP}}$ as the location of a branch point. Recall that Eq. (28) represents an isothermal sonic point (ISP). In a steady isothermal flow, a Mach number larger than \mathcal{M}_{ISP} can result in an isothermal shock such as those that may occur within radiative shocks predicted by the equilibrium diffusion model [13]. Because the pre- and post-shock Mach numbers of an isothermal shock must straddle \mathcal{M}_{ISP} , for the equilibrium diffusion model, an ISP is always located within an isothermal shock.

For nonequilibrium diffusion, the situation is more complicated. Isothermal shocks are not present, but instead discontinuities satisfy the full hydrodynamic jump conditions (12). If there is an ISP, then it cannot be in the precursor because $\mathcal{M}_0 > \mathcal{M}_p > 1$, assuming $\gamma \geq 1$ and that \mathcal{M} is monotone. The ISP is located within the hydrodynamic shock if $\mathcal{M}_s < \mathcal{M}_{\text{ISP}}$. An ISP exists in the relaxation region if $\mathcal{M}_s > \mathcal{M}_{\text{ISP}} > \mathcal{M}_1$.

Note that the ISP also plays a critical role in recombination fronts [19].

4.5 Conditions for an ISP

From Refs. [13, 21], an isothermal shock exists in the equilibrium diffusion profile whenever $\eta_1 < \eta_{\text{ISP}}$, where $\eta = 1/\rho$ and η_{ISP} satisfies (see Ref. [13, Eq. (29)])

$$\alpha(\gamma\eta_{\text{ISP}}^2\mathcal{M}_0^2)^4 = 1 + \alpha + (1 - 2\eta_{\text{ISP}})\gamma\mathcal{M}_0^2 \quad (29)$$

and $\alpha = \gamma\mathcal{P}_0/3$. We will now show that the condition for an isothermal shock may be expressed alternatively as $\mathcal{M}_1 < \mathcal{M}_{\text{ISP}}$, which is the condition for an ISP in the nonequilibrium

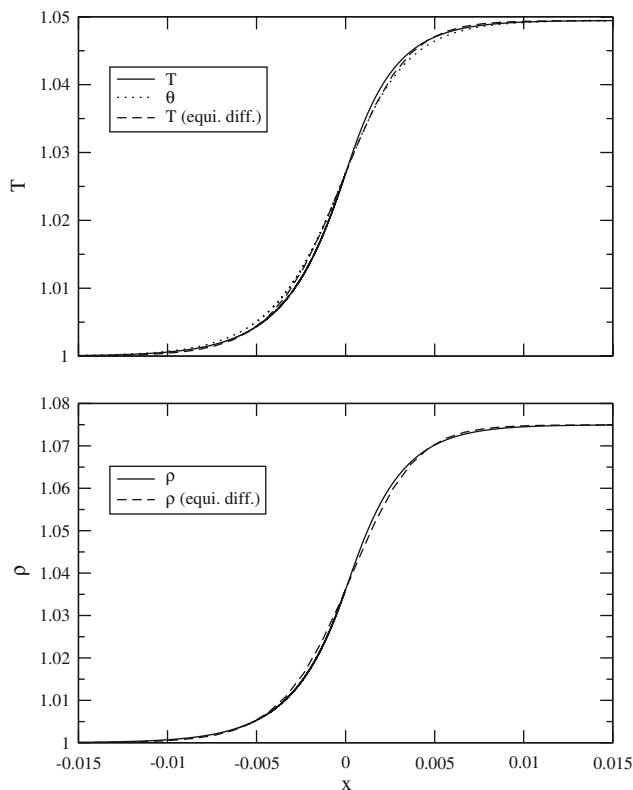


Fig. 4 Temperature and density profiles for $\mathcal{M}_0 = 1.05$, with other parameters as in Fig. 3. The equilibrium diffusion results (“equi. diff.”) were generated using the procedure from Ref. [13]. There is no isothermal sonic point (ISP) or embedded hydro shock; this case satisfies $\mathcal{M}_0 < \mathcal{M}_{0,A}$ in Fig. 3

profile. From Eq. (14),

$$T = \left(\eta \frac{\mathcal{M}_0}{\mathcal{M}} \right)^2, \quad (30)$$

so that

$$T_{\text{ISP}} = \gamma (\eta_{\text{ISP}} \mathcal{M}_0)^2. \quad (31)$$

Any point on the Hugoniot of Sect. 4.1 satisfies (see Ref. [13, Eq. (28)])

$$T - \eta + \alpha \eta (T^4 - 1) = \gamma \eta (1 - \eta) \mathcal{M}_0^2. \quad (32)$$

If we evaluate this expression at $(T, \eta) = (T_{\text{ISP}}, \eta_{\text{ISP}})$, using Eq. (31), we obtain Eq. (29). Note that in Ref. [13], Eq. (29) was derived by maximizing $T(\eta)$ in Eq. (32). The condition $\mathcal{M}_1 < \mathcal{M}_{\text{ISP}}$ for an isothermal shock is not surprising, because an isothermal shock requires a post-shock Mach number that is less than \mathcal{M}_{ISP} .

In summary, the end-state conditions for an isothermal shock in the equilibrium diffusion profile will result in an ISP for the nonequilibrium diffusion profile. Therefore, the conditions derived in Ref. [13] for the existence of an isothermal

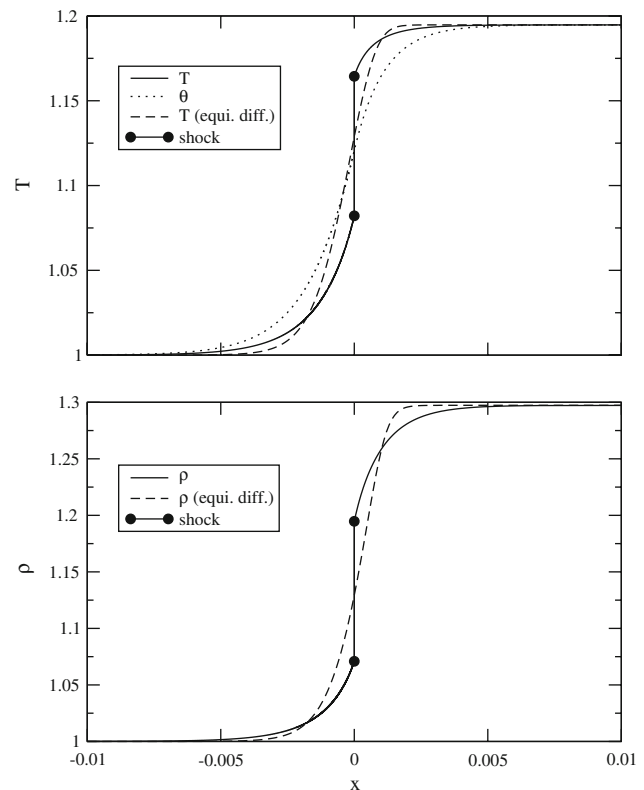


Fig. 5 Same conditions as Fig. 4, but with $\mathcal{M}_0 = 1.2$. There is a hydro shock, but no ISP; this case is in the range $\mathcal{M}_{0,A} < \mathcal{M}_0 < \mathcal{M}_{0,B}$ in Fig. 3

shock carry over to the existence of an ISP in the nonequilibrium profile.

4.6 Mach number as the independent variable

In this section, we change the independent variable from x to \mathcal{M} . Using \mathcal{M} as the independent variable will allow us to integrate easily through an ISP and to treat singularities. It follows from Eq. (14) that

$$\mathcal{M}' = -\mathcal{M} \left(\frac{\rho'}{\rho} + \frac{1}{2} \frac{T'}{T} \right), \quad (33)$$

so that

$$\frac{dx}{d\mathcal{M}} = \frac{-2\rho T}{\mathcal{M}(2T\rho' + \rho T')}. \quad (34)$$

Next, use Eq. (22) to obtain

$$\frac{dx}{d\mathcal{M}} = \frac{-6\rho T(\gamma \mathcal{M}^2 - 1)}{\mathcal{M}[8\gamma \mathcal{P}_0 \theta^3 \theta' + 3\rho(\gamma \mathcal{M}^2 + 1)T']}. \quad (35)$$

In addition,

$$\frac{dT}{d\mathcal{M}} = \frac{dx}{d\mathcal{M}} T'. \quad (36)$$

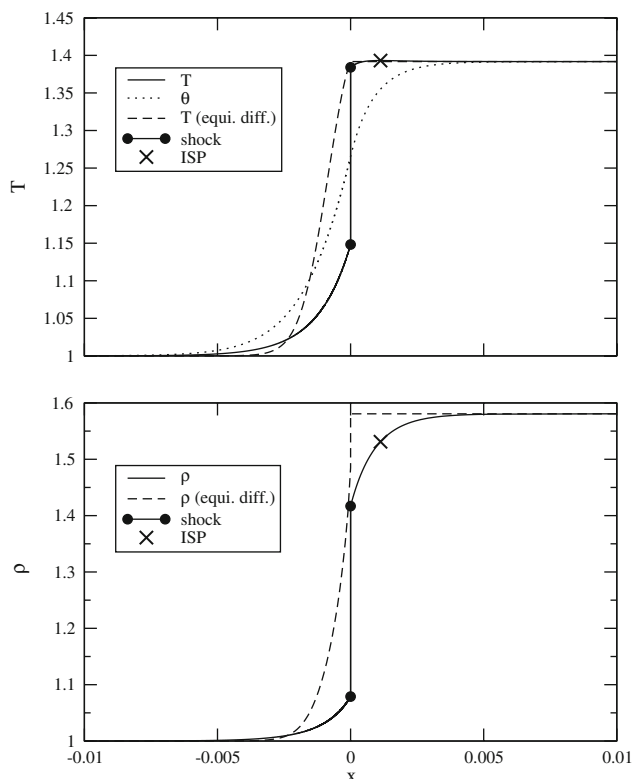


Fig. 6 Same conditions as Fig. 4, but with $\mathcal{M}_0 = 1.4$. The ISP is downstream of the hydro shock; this case is in the range $\mathcal{M}_{0,B} < \mathcal{M}_0 < \mathcal{M}_{0,C}$ in Fig. 3

Substitute Eq. (23) into Eqs. (35, 36) to yield

$$\frac{dx}{d\mathcal{M}} = -6 \frac{\mathcal{M}_0 \rho T}{(\gamma + 1) \mathcal{P}_0 \mathcal{M}} \left(\frac{\mathcal{M}^2 - 1}{Z_D} \right), \quad (37)$$

$$\frac{dT}{d\mathcal{M}} = -2 \left(\frac{\gamma - 1}{\gamma + 1} \right) \left(\frac{T}{\mathcal{M}} \right) \left(\frac{Z_N}{Z_D} \right). \quad (38)$$

where

$$Z_D = 4\mathcal{M}_0 \theta^3 \theta' + \left(\frac{\gamma - 1}{\gamma + 1} \right) (\gamma \mathcal{M}^2 + 1) r. \quad (39)$$

Although one may also substitute Eq. (18) into Eqs. (24, 39) for θ' , there is no apparent simplification.

Equations (37, 38) represent an alternative system to Eqs. (18, 23) but require that we write ρ and θ in terms of T and \mathcal{M} . Equation (14) gives that

$$\rho(T, \mathcal{M}) = \frac{\mathcal{M}_0}{\mathcal{M} \sqrt{T}}. \quad (40)$$

Also, Eq. (15) may be solved for θ :

$$\theta(T, \mathcal{M})^4 = \frac{1}{\gamma \mathcal{P}_0} \left[K_m - 3\gamma \frac{\mathcal{M}_0^2}{\rho(T, \mathcal{M})} - 3T\rho(T, \mathcal{M}) \right]. \quad (41)$$

In summary, using \mathcal{M} as the independent variable results in the following:

- Equations (40, 41) do not require the choice of a branch cut, unlike Eq. (17). This greatly simplifies the numerical integration procedure.
- Given integration endpoints $\mathcal{M} = \mathcal{M}_A$ and $\mathcal{M} = \mathcal{M}_B$, we must assume that \mathcal{M} is monotone between \mathcal{M}_A and \mathcal{M}_B . However, the validity of this assumption is easily checked because x is updated via Eq. (37). If the resulting x is non-monotone, then our assumption is violated. We have yet to encounter non-monotone behavior.
- Equations (37, 38) are singular whenever the solution is constant which occurs as $x \rightarrow \pm\infty$. Consequently, some other method must be used near the end states. This issue is discussed in the next section.
- Equations (37, 38) appear nonsingular at $\mathcal{M} = 1$, unlike Eq. (23). However, we have found that both Z_N and Z_D vanish as $\mathcal{M} \rightarrow 1$ in such a way that T' and $dT/d\mathcal{M}$ remain bounded. The treatment of this singularity is discussed in Appendix B.

5 Solution procedure

We seek to solve Eqs. (37, 38) as an initial value problem. In all of our calculations, we found that both of the end states are saddle points. Therefore, we found it necessary to integrate away from state-0 in the $+x$ -direction, in order to find the precursor region. Then, we integrate away from state-1 in the $-x$ -direction to find the relaxation region. These two branches either join to form a continuous solution or are connected by a hydrodynamic shock.

One difficulty is that at state-0 and state-1, Eqs. (37, 38) are singular and $T' = \theta' = 0$. Therefore, we require some method of starting the solution from the end states. We follow a procedure similar to Ref. [18] and evaluate $dT/d\theta$ at the end states. The relation for $dT/d\theta$ is derived in Appendix A.

Knowing $(dT/d\theta)_i$, $i = 0, 1$, we can start the integration as follows. First, we perturb θ from θ_i as

$$\theta_\varepsilon = \theta_i + \varepsilon, \quad (42)$$

where we select $|\varepsilon| \ll 1$. We assume that θ is monotone, so that for state-0 we use $\varepsilon > 0$, while for state-1 we use $\varepsilon < 0$. The corresponding temperature may be estimated as

$$T_\varepsilon = T_i + \varepsilon \left(\frac{dT}{d\theta} \right)_i, \quad (43)$$

which is accurate to $O(\varepsilon^2)$. Knowing T_ε and θ_ε , we may find the corresponding ρ_ε from Eq. (17) and assuming that ε is small enough that we remain on the branch of state- i . Finally, v_ε may be found from Eq. (13). Using $(\rho, v, T, \theta)_\varepsilon$ as the initial state, we can now integrate Eqs. (37, 38) numerically.

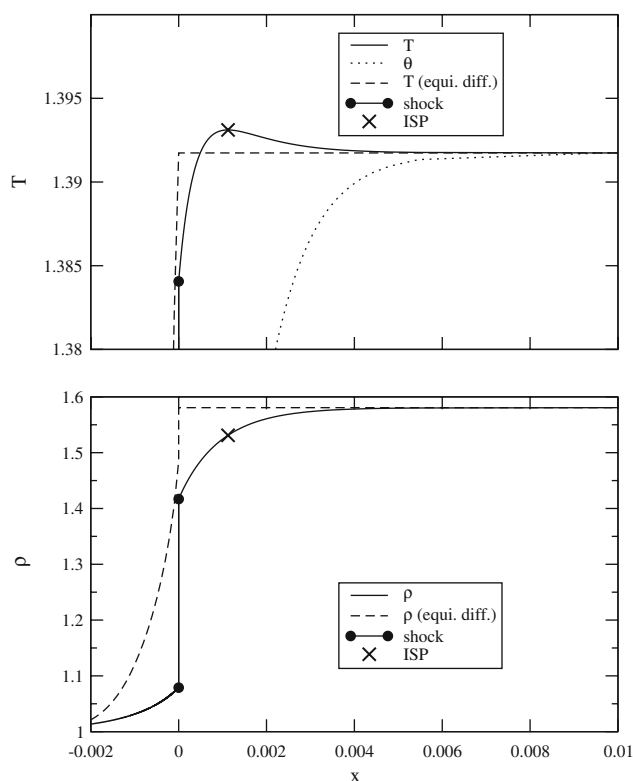


Fig. 7 Spike region of Fig. 6

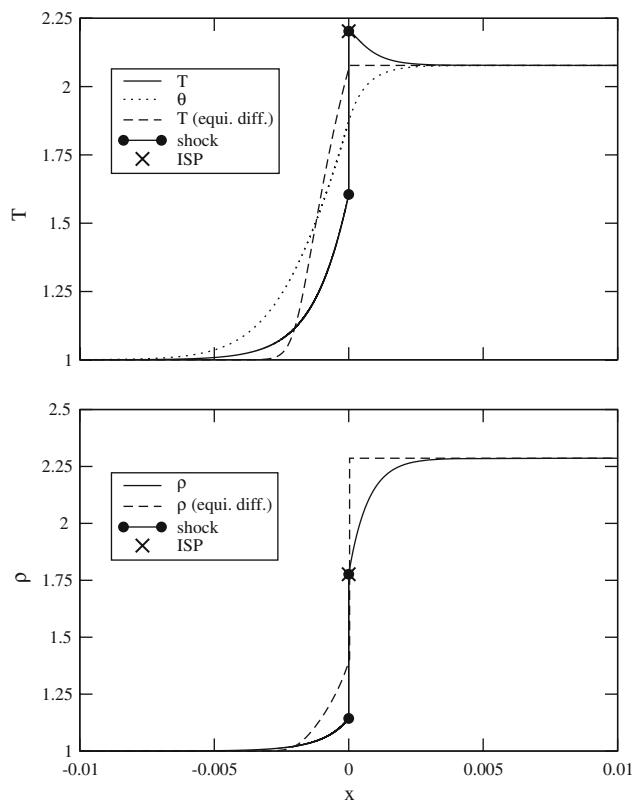


Fig. 8 Same conditions as Fig. 4, but with $\mathcal{M}_0 = 2$. The ISP is coincident with the hydro shock; this case is in the range $\mathcal{M}_{0,C} < \mathcal{M}_0 < \mathcal{M}_{0,D}$ in Fig. 3

For the exact solution, state-0 is attained as $x \rightarrow -\infty$. However, we can approximate the value of x where the solution is near state-0, which we denote as x_0 . We first compute θ'_ε using Eq. (18). Assuming that $\theta(x)$ varies linearly from $x = x_\varepsilon$ to $x = x_0$, we have that

$$x_0 = x_\varepsilon - \varepsilon/\theta'_\varepsilon. \quad (44)$$

One is free to specify x_ε . It follows that the exact solution at $x = x_0$ is within $O(\varepsilon^2)$ of state-0. We use a similar procedure to find the location where the solution is near state-1.

Figure 2 gives an overview of the steps in the solution procedure, for a case with an embedded hydrodynamic shock (this case corresponds to Fig. 8). The procedure may be summarized as follows:

1. Find $(\rho, v, T)_1$ by solving the system (8) as in Ref. [13]. Set $\theta_1 = T_1$.
2. Integrate the precursor region:
 - Find $(\rho, v, T, \theta)_\varepsilon$ using Eqs. (13, 17, 42, 43, 54).
 - Set $x_\varepsilon = 0$. Compute x_0 from Eq. (44) and set the solution at this location to state-0.
 - Find the remainder of the precursor by integrating Eqs. (37, 38) from state- ε to $\mathcal{M} = 1 + \varepsilon_{\text{ASP}}$ (or until $\theta > T_1$), where $0 < \varepsilon_{\text{ASP}} \ll 1$. In physical space, the integration is in the $+x$ -direction. The parameter ε_{ASP} is chosen large enough to avoid the adiabatic sonic point singularity discussed in Appendix B.
3. Integrate the relaxation region in the same way as the precursor region, but from $\mathcal{M} = \mathcal{M}_1$ to $\mathcal{M} = 1 - \varepsilon_{\text{ASP}}$ (or until $\theta < 1$). In physical space, the integration is in the $-x$ -direction. The relaxation region is the right two curves of the top plot in Fig. 2.
4. Next, the precursor and relaxation regions are connected. There are two possibilities:

- *Continuous case:* If

$$\theta|_{\mathcal{M}=1+\varepsilon_{\text{ASP}}} < \theta|_{\mathcal{M}=1-\varepsilon_{\text{ASP}}}, \quad (45)$$

then the solution is assumed continuous in all variables at the adiabatic sonic point. The sonic point solution is then computed with the procedure described in Appendix B. Then, the sonic point is placed at $x = 0$ and the endpoints of the precursor and relaxation region are connected at this point. See Appendix B for more details.

- *Embedded shock case:* Otherwise, a hydrodynamic shock connects the two regions. The hydro shock is placed at $x = 0$ and the regions are translated in x such that the θ -values are continuous and the density discontinuity satisfies the hydrodynamic jump conditions of Sect. 4.2. See the bottom plot of Fig. 2.

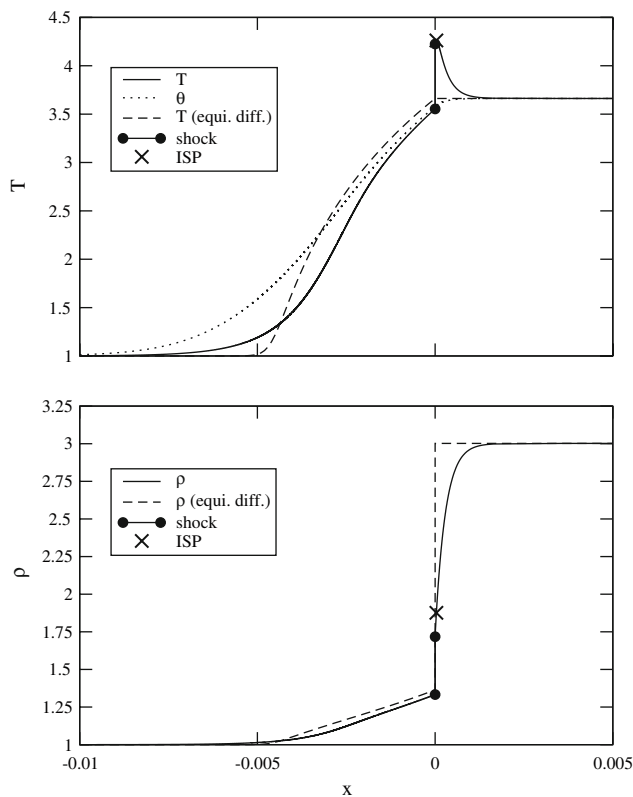


Fig. 9 Same conditions as Fig. 4, but with $\mathcal{M}_0 = 3$. The ISP is downstream of the hydro shock; this case is in the range $\mathcal{M}_{0,D} < \mathcal{M}_0 < \mathcal{M}_{0,E}$ in Fig. 3

6 Results

In this section, we present several example radiative shock solutions. First consider a constant cross-section case, with $\mathcal{P}_0 = 10^{-4}$, $\gamma = 5/3$, $\sigma_a = 10^6$, and $\kappa = 1$. Figure 3 shows \mathcal{M}_1 and \mathcal{M}_s for a range of \mathcal{M}_0 . As a reminder, \mathcal{M}_s is the post-hydro shock Mach number and $\mathcal{M}_s = 1$ is used to indicate that there is no hydro shock in the profile. Note that \mathcal{M}_1 is solely a function of the overall jump conditions presented in Sect. 4.1, while the results here for \mathcal{M}_s are specific to the nonequilibrium diffusion model. In all of our solutions, \mathcal{M} decreases monotonically from \mathcal{M}_0 to \mathcal{M}_1 . Therefore, in the relaxation region, \mathcal{M} decreases monotonically from \mathcal{M}_s to \mathcal{M}_1 .

The labels “A” through “G” in Fig. 3 denote certain transition points in the solution behavior. Figures 4, 5, 6, 7, 8, 9, 10, 11, 12, 13, 14, 15, 16 show the temperature and density profiles at values of \mathcal{M}_0 that are between the transition points. The results are compared with the equilibrium diffusion results of Ref. [13]. The nonequilibrium diffusion solutions are characterized primarily by the following:

- Is there an embedded hydrodynamic shock? If no, then the solution is continuous in all variables. For the conditions

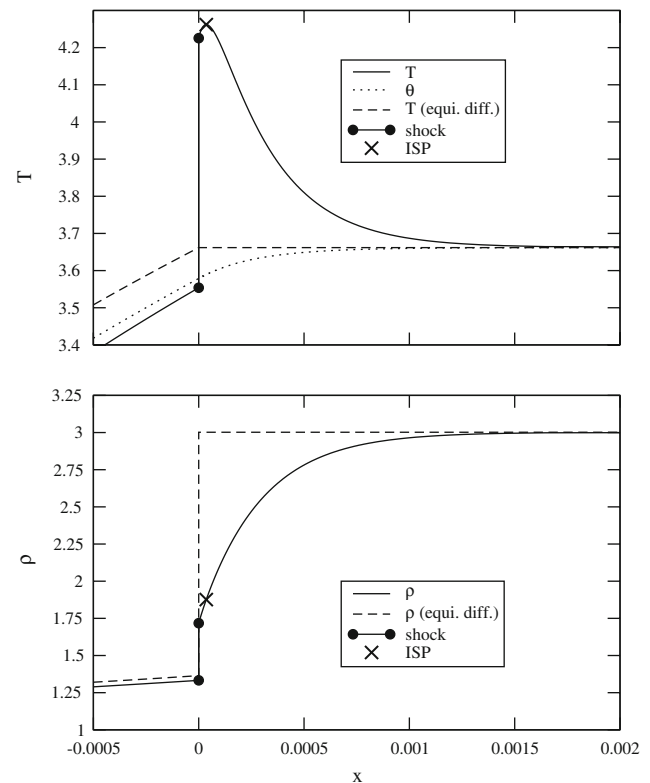


Fig. 10 Spike region of Fig. 9

in Fig. 3, there is a hydrodynamic shock between points “A” and “E”, where $\mathcal{M}_s < 1$. See also Figs. 5, 6, 7, 8, 9, 10, 11, 12, 13. Continuous solutions are found for small \mathcal{M}_0 (Fig. 4) and large \mathcal{M}_0 (Figs. 14, 15, 16).

- Is there an isothermal sonic point (ISP)? If yes, then we found that the maximum temperature exceeds T_1 ; that is, there is a Zel’dovich spike. The spike location occurs near the ISP and this will be discussed further in the next section. For the conditions in Fig. 3, there is an ISP between points “B” and “F”, where $\mathcal{M}_1 < \mathcal{M}_{\text{ISP}}$. See Figs. 6, 7, 8, 9, 10, 11, 12, 13, 14, 15 for examples.

We stress that unlike previous work, the existence of the Zel’dovich spike is a result of the ISP, as opposed to the existence of an embedded hydrodynamic shock.

When there is an embedded hydrodynamic shock, there are cases where the ISP is coincident with the shock ($\mathcal{M}_s \leq \mathcal{M}_{\text{ISP}}$), which occurs between points “C” and “D” in Fig. 3. In this range of \mathcal{M}_0 , the maximum temperature occurs at the hydrodynamics shock; see Fig. 8. But there are also cases where the ISP, and thus the maximum temperature, is downstream of the shock ($\mathcal{M}_s > \mathcal{M}_{\text{ISP}}$). In Fig. 3, this occurs between points “B” and “C” (see Figs. 6, 7) and between points “D” and “E” (see Figs. 9, 10, 11, 12, 13).

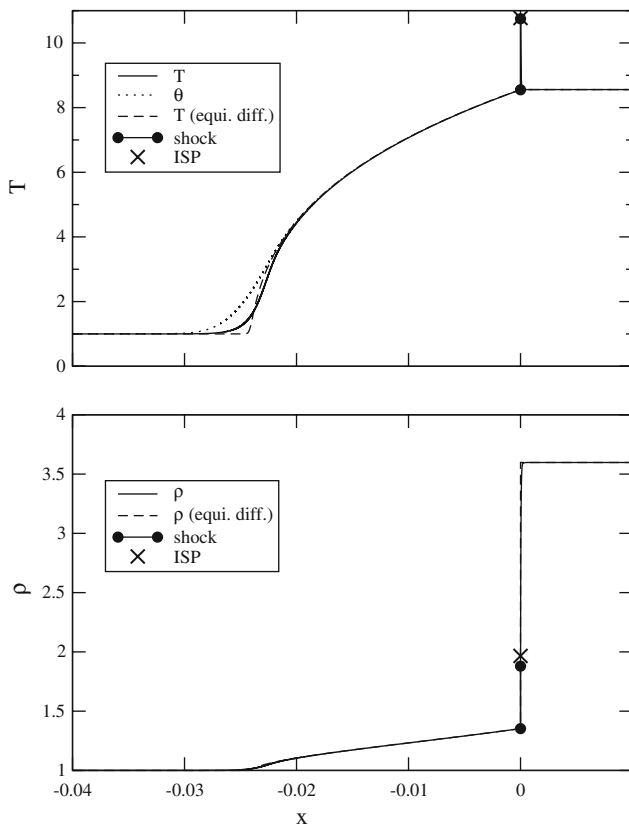


Fig. 11 Same conditions as Fig. 4, but with $\mathcal{M}_0 = 5$. Supercritical, with ISP downstream of hydro shock; this case is in the range $\mathcal{M}_{0,D} < \mathcal{M}_0 < \mathcal{M}_{0,E}$ in Fig. 3

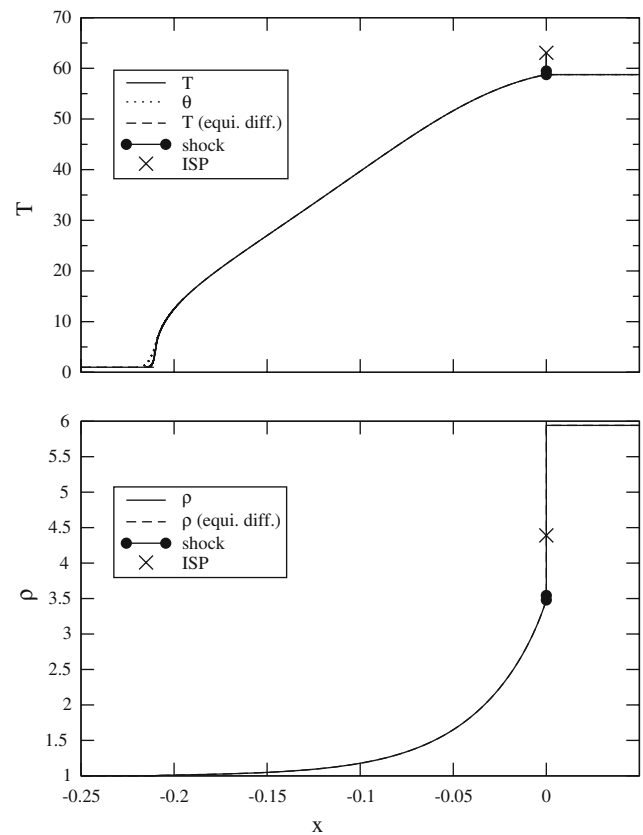


Fig. 12 Same conditions as Fig. 4, but with $\mathcal{M}_0 = 27$. The ISP is downstream of the hydro shock; this case is in the range $\mathcal{M}_{0,D} < \mathcal{M}_0 < \mathcal{M}_{0,E}$ in Fig. 3

Without a hydrodynamic shock, an ISP may still exist, which occurs between points “E” and “F” in Fig. 3. The resulting temperature spike is shown in Figs. 14 and 15. Between points “A” and “B” in Fig. 3, there is a hydrodynamic shock but no ISP. Therefore, $T_s < T_1$; see Fig. 5.

For the conditions of Fig. 3, the transition from a subcritical shock ($T_p < T_1$) to a supercritical shock ($T_p = T_1$) occurs somewhere between $\mathcal{M}_0 = 3$ and $\mathcal{M}_0 = 5$; see Figs. 9, 10, 11. Generally, for the subcritical cases, the entire shock profile is out of equilibrium, and thus the nonequilibrium and equilibrium diffusion results differ significantly. For the supercritical cases, much of the precursor region is near equilibrium, except at its foot. But the equilibrium diffusion cannot predict the temperature spike region, as this is a nonequilibrium feature. At very high \mathcal{M}_0 , such as the $\mathcal{M}_0 = 50$ case in Fig. 16, there is no spike and the equilibrium theory matches nonequilibrium diffusion very well.

In Refs. [1, 13], a quantitative range of \mathcal{M}_0 and \mathcal{P}_0 values were found to result in an embedded isothermal shock in the equilibrium diffusion limit. For $\mathcal{P}_0 < O(1)$, an isothermal shock exists in the range

$$\mathcal{M}_{\text{iso}} < \mathcal{M}_0 < \mathcal{M}_{\text{cont}}, \quad (46)$$

where accurate estimates for \mathcal{M}_{iso} and $\mathcal{M}_{\text{cont}}$ are derived in Ref. [13]. Referring to Fig. 3, $\mathcal{M}_0 = \mathcal{M}_{\text{iso}}$ corresponds to point “B”, while $\mathcal{M}_0 = \mathcal{M}_{\text{cont}}$ corresponds to point “F”. An isothermal shock is clearly present in the equilibrium diffusion density profiles of Figs. 6, 7, 8, 9, 10, 11, 12, 13, 14, 15. As discussed in Sect. 4.5 and the results above, the range (46) will result in an ISP for nonequilibrium diffusion. Note that $\mathcal{M}_{\text{cont}} \rightarrow \infty$ in the low energy density limit.

The value $\mathcal{P}_0 = 10^{-4}$ may appear small for a “high energy density” flow. However, regardless of the value of \mathcal{P}_0 , the post-shock conditions are high energy density whenever $\mathcal{M}_0 \approx \mathcal{M}_{\text{cont}}$ and result in $\mathcal{P}_1 = O(1)$ [1, 13]. If we take $\tilde{L} = 1$ cm, $\tilde{\rho}_0 = 1$ g/cc, and zero scattering ratio, the nondimensional parameters we have chosen correspond to $\tilde{T}_0 \approx 122$ eV. Larger values of \mathcal{P}_0 increase \tilde{T}_0 , but decrease $\mathcal{M}_{\text{cont}}$, so that for $\mathcal{P}_0 \gtrsim 2.53$, the ISP and hydrodynamic shock are not present at any \mathcal{M}_0 [13]. Thus, a smaller value of \mathcal{P}_0 results in a richer variety of solution regimes.

In Fig. 3, we see that $\mathcal{M}_1 > 1$ whenever $\mathcal{M}_0 > \mathcal{M}_{0,G}$. This result appears to violate the standard hydrodynamic entropy condition. However, the Mach number in this study is defined with respect to the material sound speed. Equilibrium radiation increases the effective sound speed (see

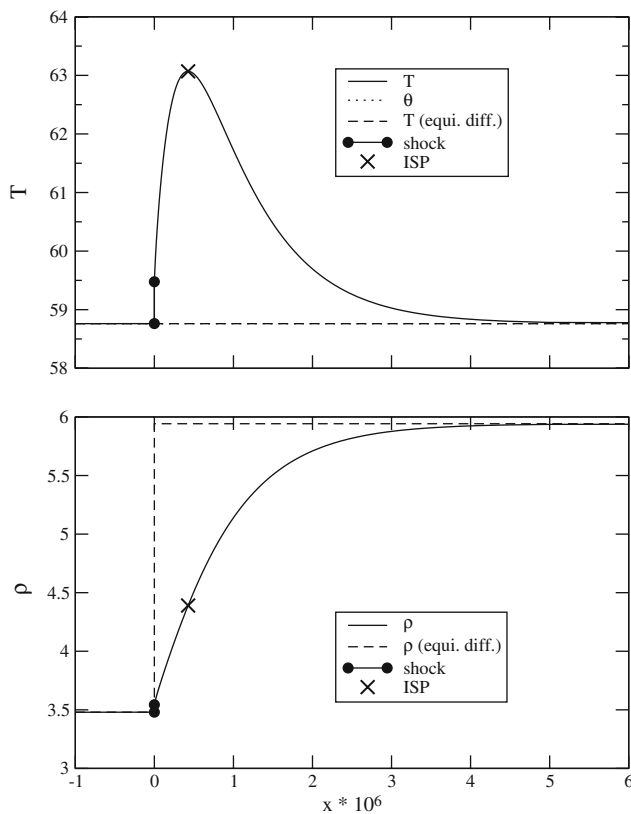


Fig. 13 Spike region of Fig. 12

Refs. [14, Eq. (101.22)] and [11]) and it does so in such a way that the Mach number defined with respect to the radiation-modified sound speed is always less than unity at state-₁. The radiation-modified entropy is always greater at state-₁ than state-₀.

Figure 17 shows the effect of using variable cross-sections, whose functional dependence is a simple model of bremsstrahlung [21]. These results should be compared with Fig. 11 and show that the foot of the precursor is steepened.

Finally, Fig. 18 shows the effect of increasing \mathcal{P}_0 from 0.0001 to 0.1, for $\mathcal{M}_0 = 2$. The increased radiation has the effect of regularizing the solution to the point of eliminating the embedded hydro shock. The ISP is still present resulting in a significant temperature spike. At $\mathcal{M}_0 = 2$, the ISP is absent for $\mathcal{P}_0 \gtrsim 1.01$.

7 Maximum temperature

In this section, we explain why the maximum temperature occurs near the isothermal sonic point (ISP) and derive an estimate for its value. Given the results of the previous section, a reasonable approximation is that $\theta' \approx 0$ in the Zel'dovich spike region so that Eq. (38) reduces to

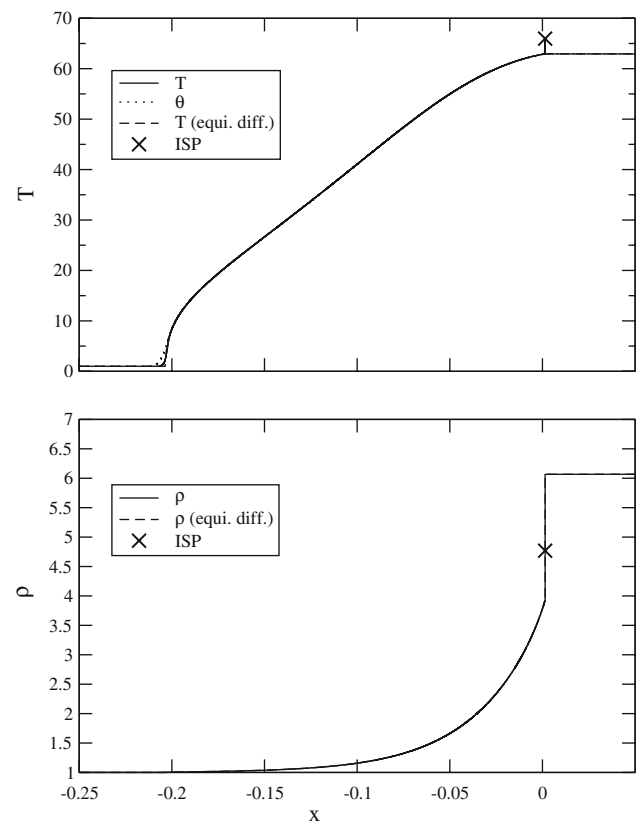


Fig. 14 Same conditions as Fig. 4, but with $\mathcal{M}_0 = 30$. No embedded hydro shock, but contains an ISP; this case is in the range $\mathcal{M}_{0,E} < \mathcal{M}_0 < \mathcal{M}_{0,F}$ in Fig. 3

$$\frac{dT}{d\mathcal{M}} \approx -\frac{2T}{\mathcal{M}} \frac{\mathcal{M}^2 - \mathcal{M}_{\text{ISP}}^2}{\mathcal{M}^2 + \mathcal{M}_{\text{ISP}}^2}. \quad (47)$$

The θ' term also vanishes under the assumption of low-energy density.

It follows from Eq. (47) that T reaches its maximum value when $\mathcal{M} \approx \mathcal{M}_{\text{ISP}}$. In other words, the maximum T occurs near the ISP as shown in Figs. 8, 9, 10, 11, 12, 13, 14, 15. Keep in mind that the maximum temperature is not *exactly* at the ISP, because of the assumption $\theta' \approx 0$. This assumption is questionable for small \mathcal{M}_0 (see Fig. 8), but we will be able to quantify this error below. Also, in the low energy density approximation, the θ' term is absent in Eq. (38), and so the maximum temperature is exactly at the ISP.

For the $\mathcal{M} = 2$ case shown in Fig. 8, we find that $\mathcal{M}_s < \mathcal{M}_{\text{ISP}}$, so that T decreases monotonically in the relaxation region. In this case, the ISP is located within the hydrodynamic shock, because $\mathcal{M}_p > 1 > \mathcal{M}_{\text{ISP}} > \mathcal{M}_s$.

We may also estimate the maximum temperature of the spike, denoted as T_{max} . If we assume that the maximum temperature occurs at $\mathcal{M} = \mathcal{M}_{\text{ISP}}$, then Eq. (26) holds. Also, we assume that $\theta = T_1$ at the spike, which is consistent with our assumption that $\theta' \approx 0$. With these assumptions, if we then solve Eq. (26) for T , we obtain

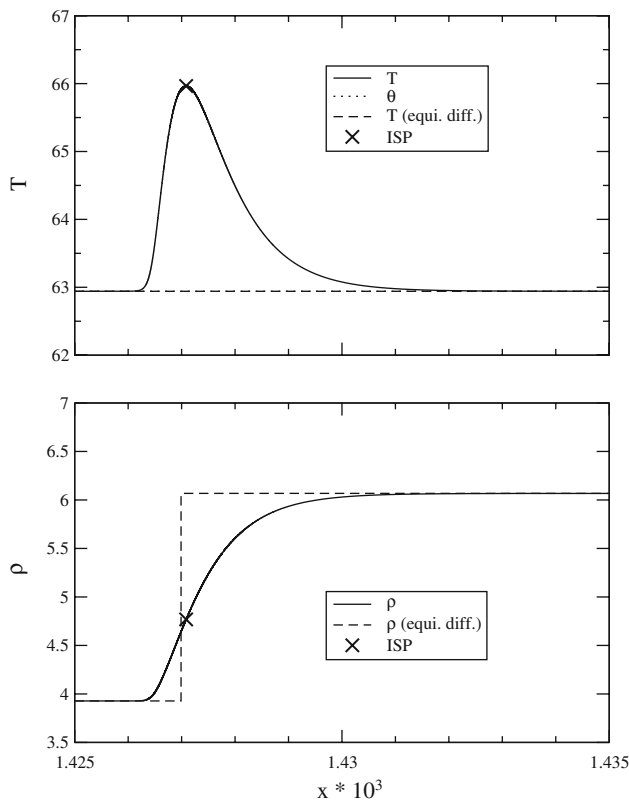


Fig. 15 Spike region of Fig. 14

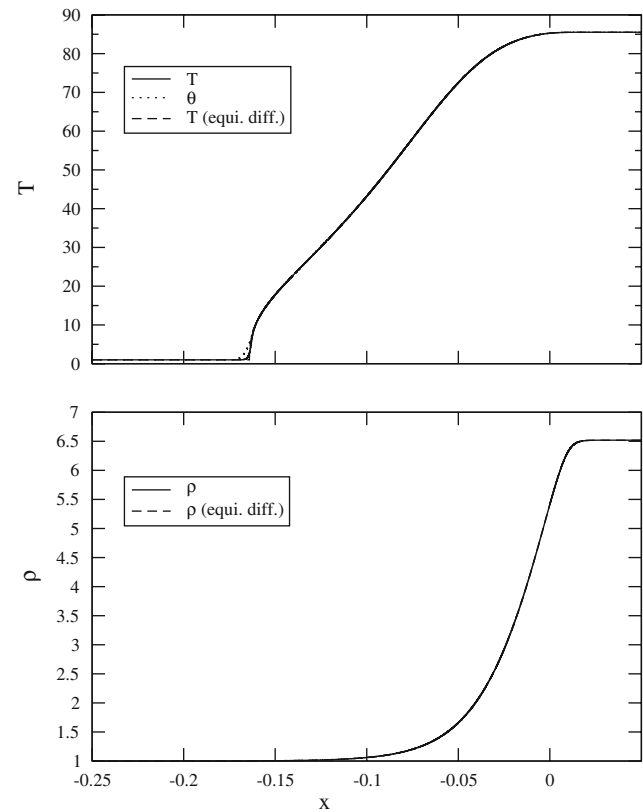


Fig. 16 Same conditions as Fig. 4, but with $\mathcal{M}_0 = 50$. No embedded hydro shock or ISP; this case satisfies $\mathcal{M}_0 > \mathcal{M}_{0,F}$ in Fig. 3

$$T_{\max} = \max \left\{ T_1, \frac{[3(\gamma \mathcal{M}_0^2 + 1) + \gamma \mathcal{P}_0(1 - T_1^4)]^2}{36\gamma \mathcal{M}_0^2} \right\}. \quad (48)$$

In this relation, we restrict $T_{\max} \geq T_1$ in order to handle cases that do not have an ISP; it can be shown that the above relation gives $T_{\max} > T_1$ only when $\mathcal{M}_1 < \mathcal{M}_{1,\text{ISP}}$.

Mihalas and Mihalas [14] derived the estimate

$$T_{\max}(\text{Mihalas}) = (3 - \gamma)T_1. \quad (49)$$

Equations (48) and (49) are compared in Fig. 19, along with values from taken from the solutions of the previous section. Clearly, Eq. (48) is a very accurate estimate compared with nonequilibrium diffusion results, whereas Eq. (49) is a rough upper bound. Note that Eq. (48) requires no knowledge of the cross-sections or radiation model. Finally, the estimate remains accurate at low \mathcal{M}_0 , where our assumptions are most questionable.

The rise in temperature that may occur after (or in absence of) the hydrodynamic shock may not be intuitive. We offer the following qualitative, albeit incomplete, explanation. The post-shock temperature rise is very pronounced in the $\mathcal{M}_0 = 27$ case of Figs. 12 and 13. One reason for the temperature

rise here becomes apparent, if one studies the corresponding density profile. Recall that for $\gamma = 5/3$, the maximum compression for a hydrodynamic shock is $\rho_1/\rho_0 = 4$. Adding radiative effects to this case increases this compression by approximately 50%, with most of the additional compression taking place after the embedded hydro shock. This additional compression further increases the material temperature, until radiative cooling takes over to relax the temperature back to $T = T_1$.

We also know that in the optically-thick limit, equilibrium diffusion holds. Equilibrium diffusion models discontinuities as isothermal shocks. Nonequilibrium diffusion smoothes these isothermal shocks over a length on the order of a photon mean-free-path, as shown clearly in the results of Figs. 14 and 15. The nonequilibrium material temperature cannot follow the isothermal shock Hugoniot and the result is a spike.

8 Summary

Our solutions and analysis have shown the following:

- The existence of the temperature (Zel'dovich) spike is more a result of the isothermal sonic point (ISP), rather

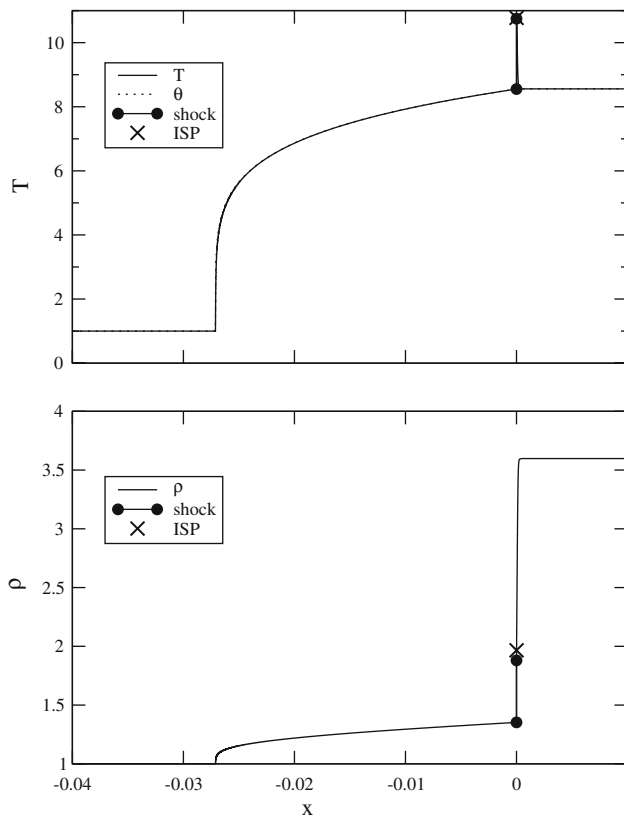


Fig. 17 Same conditions as Fig. 11, but with variable cross-sections: $\kappa = 0.00175T^{7/2}/\rho$, $\sigma_a = 10^6/\kappa$

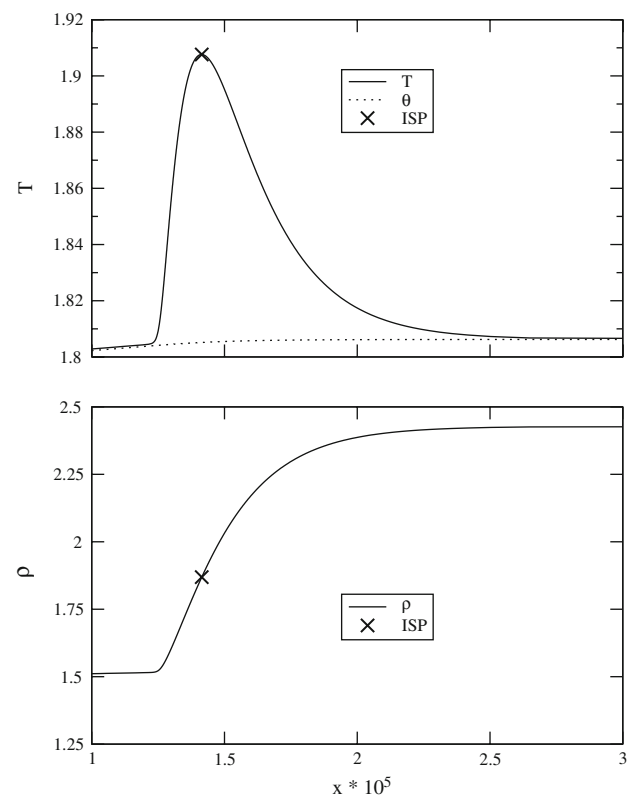


Fig. 18 Same conditions as the $\mathcal{M}_0 = 2$ case of Fig. 8, but with $\mathcal{P}_0 = 0.1$. Spike region only; no embedded hydro shock

than the embedded hydrodynamic shock. Future work should investigate how this result carries over when additional physics is added, such as separate ion and electron temperatures.

- The conditions derived in Refs. [1, 13] for the existence of an isothermal shock carry over to the existence of an ISP in the nonequilibrium profile. In order to cover all of the solution regimes, for a given \mathcal{P}_0 , one should span the range $\mathcal{M}_{\text{iso}} < \mathcal{M}_0 < \mathcal{M}_{\text{cont}}$, as in Figs. 3, 4, 5, 6, 7, 8, 9, 10, 11, 12, 13, 14, 15, 16.
- Precise estimates for the existence of an embedded hydrodynamic shock are left for future work. Even for nonequilibrium diffusion, this detail is a function of κ and σ_a , and thus we expect it also to be a function of the radiation model. Our results here show that the embedded shock may be present with or without the presence of an ISP. The embedded shock disappears at very low and very high \mathcal{M}_0 , similar to the behavior of isothermal shocks in equilibrium diffusion solutions.
- We have derived an improved estimate for T_{max} , Eq. (48). This estimate is independent of the radiation model or cross-sections. Future work should consider whether this estimate remains valid for more complicated radiation and material models.

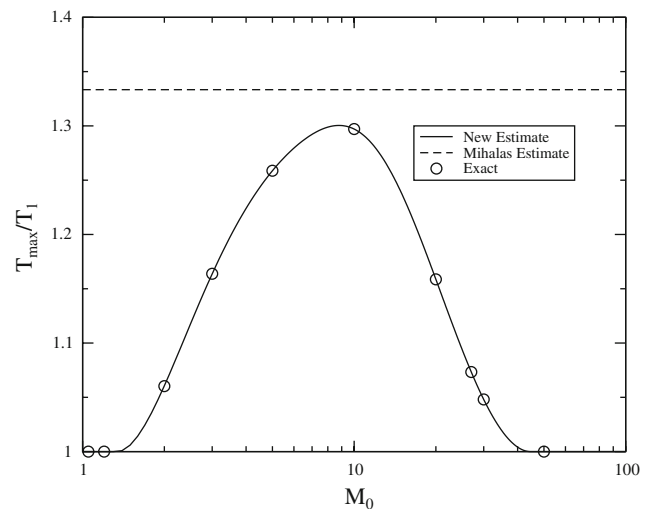


Fig. 19 T_{max}/T_1 versus \mathcal{M}_0 for $\mathcal{P}_0 = 10^{-4}$, $\gamma = 5/3$. “New Estimate” is from Eq. (48), “Mihalas Estimate” is from Eq. (49), and “Exact” values are from the nonequilibrium diffusion results of Figs. 4–16

Acknowledgments We greatly appreciate the detailed comments provided by the anonymous reviewers. This work was performed under the auspices of the US Department of Energy under contract DE-AC52-06NA25396.

Appendix A: Derivation of $(dT/d\theta)_0$ and $(dT/d\theta)_1$

In this appendix we derive an expression for $dT/d\theta$ at the end states. Let

$$T' = F(T, \theta), \quad \theta' = G(T, \theta), \quad (50)$$

where $F(T, \theta)$ and $G(T, \theta)$ are given by the right-hand sides of Eqs. (23) and (18), respectively. In general,

$$\frac{dT}{d\theta} = \frac{F(T, \theta)}{G(T, \theta)}. \quad (51)$$

The difficulty is that at state-0 and state-1, $F = G = 0$, so a limit must be taken.

At state- i we can rewrite Eq. (51) as

$$\left(\frac{dT}{d\theta}\right)_i = \lim_{\varepsilon \rightarrow 0} \frac{F(T_i + \varepsilon(dT/d\theta)_i, \theta_i + \varepsilon)}{G(T_i + \varepsilon(dT/d\theta)_i, \theta_i + \varepsilon)}; \quad i = 0, 1. \quad (52)$$

If we expand F and G about state- i , this relation simplifies to

$$\left(\frac{dT}{d\theta}\right)_i = \frac{(\partial_T F)_i (dT/d\theta)_i + (\partial_\theta F)_i}{(\partial_T G)_i (dT/d\theta)_i + (\partial_\theta G)_i}; \quad i = 0, 1, \quad (53)$$

where we have used the fact that $F(T_i, \theta_i) = G(T_i, \theta_i) = 0$. To this point, we have simply applied L'Hopital's rule to Eq. (50). The above equation is a quadratic in $(dT/d\theta)_i$ whose solution is

$$\frac{dT}{d\theta} = \frac{\partial_T F - \partial_\theta G \pm \sqrt{(\partial_T F - \partial_\theta G)^2 + 4(\partial_T G)(\partial_\theta F)}}{2(\partial_T G)}, \quad (54)$$

where the common subscript- i has been dropped. The root is selected that gives $d\rho/d\theta > 0$.

The derivatives $\partial_T F$, $\partial_\theta F$, $\partial_T G$, and $\partial_\theta G$ are easily evaluated from Eqs. (23) and (18). We obtain

$$\partial_T G = c_1 \left\{ 6C_p \rho [2(\partial_T \rho)(T - 1) + \rho] - 6\mathcal{M}_0^2 \rho (\partial_T \rho) + 8\mathcal{P}_0 (\partial_T \rho)(\theta^4 - 2\rho) \right\}, \quad (55)$$

$$\partial_\theta G = c_1 \left\{ 12C_p (\partial_\theta \rho) \rho (T - 1) - 6\mathcal{M}_0^2 \rho (\partial_\theta \rho) + 8\mathcal{P}_0 [(\partial_\theta \rho)(\theta^4 - 2\rho) + 4\rho\theta^3] \right\}, \quad (56)$$

$$\partial_T F = c_2 \left[4v\theta^3 (\partial_T G) - 12\sigma_a (\gamma \mathcal{M}^2 - 1) T^3 \right], \quad (57)$$

$$\partial_\theta F = c_2 \left[4v\theta^3 (\partial_\theta G) + 12\sigma_a (\gamma \mathcal{M}^2 - 1) \theta^3 \right], \quad (58)$$

where

$$c_1 = \frac{\mathcal{M}_0}{24\mathcal{P}_0 \kappa \rho^2 \theta^3}, \quad (59)$$

$$c_2 = \frac{\mathcal{P}_0}{3C_p \mathcal{M}_0 (\mathcal{M}^2 - 1)}. \quad (60)$$

Note that these expressions are not general but instead take advantage of the fact that $F = G = 0$. Also, from Eq. (17),

$$\partial_T \rho = -\frac{1}{T} \left(\rho \pm \frac{3\gamma \mathcal{M}_0^2}{d} \right), \quad (61)$$

$$\partial_\theta \rho = -\frac{2}{3} \frac{\mathcal{P}_0 \gamma \theta^3}{T} \left(1 \pm \frac{K_m - \gamma \mathcal{P}_0 \theta^4}{d} \right), \quad (62)$$

where

$$d = \sqrt{b^2 - 36\gamma \mathcal{M}_0^2 T}. \quad (63)$$

The root selected is the same as for Eq. (17).

Appendix B: Sonic-point singularity

In this appendix, we describe the singularity that may occur at the adiabatic sonic point (ASP), defined as where $\mathcal{M} = 1$, and how the solution is computed in this region. If there is an embedded hydrodynamic shock, then the ASP must be within this shock and the jump conditions described in Sect. 4.2 apply in a straightforward manner. The issue is whenever conditions are such that the solution is continuous; that is, whenever there is no embedded hydrodynamic shock. In this case, our numerical results suggest that the expressions for T' , $dT/d\mathcal{M}$, and $dx/d\mathcal{M}$ [see Eqs. (23, 38, 37)] have a removable singularity (zero divided by zero and bounded) at the ASP. Specifically, we assume that for continuous solutions, the values for Z_N and Z_D , given by Eqs. (24, 39), vanish as $\mathcal{M} \rightarrow 1$ in such a way that T' , $dT/d\mathcal{M}$, and $dx/d\mathcal{M}$ remain bounded. We leave a mathematical proof that this singularity exists for future work. In this appendix, we assume simply that the singularity is present and then derive a procedure for computing the solution in this region.

With the assumption that Z_N vanishes at the ASP, we may compute the temperature at this point. Because $Z_N = Z_N(T, \mathcal{M})$, the temperature satisfies

$$Z_N(T_{\text{ASP}}, 1) = 0. \quad (64)$$

We use a numerical root-finding algorithm in order to solve this expression for T_{ASP} . Knowing that $\mathcal{M} = 1$ and $T = T_{\text{ASP}}$, the remainder of the solution state at the ASP may be found using Eqs. (14, 40, 41). It may be surprising that we can find the solution at the ASP without integrating Eq. (38). However, we stress that Eq. (64) is valid only when the solution is continuous. The solution is continuous if the condition (45) is satisfied and evaluation of this condition requires integrating Eq. (38).

Without a loss of generality, we place the ASP at $x = 0$. What remains is to place the precursor and relaxation regions, computed in Steps (2) and (3) of Sect. 5, relative to $x = 0$. Let the subscript- L denote the solution at $\mathcal{M} = 1 + \varepsilon_{\text{ASP}}$, which is the integration endpoint of the precursor found in

Step (2) of Sect. 5. Similarly, let the subscript- R denote the solution at $\mathcal{M} = 1 - \varepsilon_{\text{ASP}}$, which is the integration endpoint of the relaxation region found in Step (3) of Sect. 5. We select ε_{ASP} large enough that Eq. (37) may be used to compute $(dx/d\mathcal{M})_{L,R}$ reliably. We then have that

$$x_L = \varepsilon_{\text{ASP}} \left(\frac{dx}{d\mathcal{M}} \right)_L, \quad (65a)$$

$$x_R = -\varepsilon_{\text{ASP}} \left(\frac{dx}{d\mathcal{M}} \right)_R, \quad (65b)$$

which are accurate to $O(\varepsilon_{\text{ASP}}^2)$. Because $\mathcal{M}(x)$ is monotonically decreasing, $x_L < 0 < x_R$. The precursor region is then translated such that $x = x_L$ at $\mathcal{M} = 1 + \varepsilon_{\text{ASP}}$ and the relaxation region is translated such that $x = x_R$ at $\mathcal{M} = 1 - \varepsilon_{\text{ASP}}$. This completes the solution procedure for continuous solutions.

Additional accuracy may be obtained if we use the value for $dx/d\mathcal{M}$ at the ASP, but this requires applying L'Hopital's rule to Eq. (37). The resulting expression is quite complicated. We found that using Eqs. (65) is much simpler and is sufficiently accurate.

References

- Bouquet, S., Teyssier, R., Chieze, J.P.: Analytical study and structure of a stationary radiative shock. *Astrophys. J. Suppl. Ser.* **127**(2), 245–252 (2000)
- Brunner, T.A., Mehlhorn, T.A.: A user's guide to radiation transport in ALEGRA-HEDP, Version 4.6. Technical report, SAND2004-5799, Sandia National Laboratories (2004)
- Coggeshall, S.V., Axford, R.A.: Lie group invariance properties of radiation hydrodynamics equations and their associated similarity solutions. *Phys. Fluids* **29**(8), 2398–2420 (1986)
- Drake, R.P.: *High-Energy-Density Physics. Shock Wave and High Pressure Phenomena*. Springer, Heidelberg (2006)
- Drake, R.P.: Energy balance and structural regimes of radiative shocks in optically thick media. *IEEE Trans. Plasma Sci.* **35**(2), 171–180 (2007)
- Drake, R.P.: Theory of radiative shocks in optically thick media. *Physics of Plasmas* **14** (2007)
- Fadeyev, Y.A., Gillet, D.: The structure of radiative shock waves: II The multilevel hydrogen atom. *Astron. Astrophys.* **354**, 349–364 (2000)
- Gittings, M., Weaver, R., Clover, M., Betlach, T., Byrne, N., Coker, R., Dendy, E., Hueckstaedt, R., New, K., Oakes, W.R., Ranta, D., Stefan, R.: The RAGE radiation-hydrodynamics code. Technical report, LA-UR-06-0027, Los Alamos National Laboratory (2006)
- Hayes, J.C., Norman, M.L., Fiedler, R.A., Bordner, J.O., Li, P.S., Clark, S.E., ud Doula, A., Low, M.M.M.: Simulating radiating and magnetized flows in multiple dimensions with ZEUS-MP. *Astrophys. J. Suppl. Ser.* **165**(1), 188–228 (2006)
- Heaslet, M.A., Baldwin, B.S.: Predictions of structure of radiation-resisted shock waves. *Phys. Fluids* **6**(6), 781–791 (1963)
- Lowrie, R., Morel, J.: Issues with high-resolution Godunov methods for radiation hydrodynamics. *J. Quant. Spectrosc. Radiat. Transf.* **69**(4), 475–489 (2001)
- Lowrie, R.B., Edwards, J.D.: Shock wave solutions for radiation hydrodynamics. In: *Proceedings of the ANS joint international topical meeting on math and computations + supercomputing in nuclear applications*. American Nuclear Society, Monterey (2007)
- Lowrie, R.B., Rauenzahn, R.M.: Radiative shock solutions in the equilibrium-diffusion limit. *Shock Waves* **16**(6), 445–453 (2007)
- Mihalas, D., Mihalas, B.W.: *Foundations of Radiation Hydrodynamics*. Oxford University Press, New York (1984)
- Sincell, M.W., Gehmeyr, M., Mihalas, D.: The quasi-stationary structure of radiating shock waves. I. The one-temperature fluid. *Shock Waves* **9**(6), 391–402 (1999)
- Sincell, M.W., Gehmeyr, M., Mihalas, D.: The quasi-stationary structure of radiating shock waves. II. The two-temperature fluid. *Shock Waves* **9**(6), 403–411 (1999)
- Wang, C.P.: Effect of thermal radiation on the propagation of plane shock waves. *Phys. Fluids* **13**(7), 1717–1724 (1970)
- Weiss, W.: Structure of shock waves. In: Müller, I., Ruggeri, T. (eds.) *Rational Extended Thermodynamics*, Springer Tracts in Natural Philosophy, vol 37, 2nd edn., pp. 277–307. Springer, Heidelberg (1998)
- Williams, R.J.R., Dyson, J.E.: Breaking the sound barrier in recombination fronts. *Mon. Not. R. Astron. Soc.* **279**(3), 987–992 (1996)
- Zel'dovich, Y.B.: Shock waves of large amplitude air. *Soviet Phys. JETP* **5**(5), 919–927 (1957)
- Zel'dovich, Y.B., Raizer, Y.P.: *Physics of Shock Waves and High-Temperature Hydrodynamic Phenomena*. Dover, New York (2002)